PHYSICAL REVIEW FLUIDS **7**, 104605 (2022)

Characteristics of the intense vorticity structures in isotropic turbulence at high Reynolds numbers

A. A. Ghira,[1] G. E. Elsinga ,[2] and C. B. da Silva [1,*]
[1] *LAETA, IDMEC, Instituto Superior Técnico, Universidade de Lisboa,*
Av. Rovisco Pais, 1049-001 Lisbon, Portugal
[2] *Laboratory for Aero and Hydrodynamics, Department of Mechanical, Maritime and Materials Engineering,*
Delft University of Technology, Mekelweg 2, 2628CD Delft, The Netherlands

(Received 27 April 2022; accepted 14 September 2022; published 14 October 2022)

Direct numerical simulations (DNS) of forced (statistically stationary) isotropic turbulence are used to assess the characteristics of the intense vorticity structures (IVS) or "worms" at higher Reynolds numbers than previously available. The simulations cover a range of Taylor-based Reynolds numbers in the range $90 \leqslant \mathrm{Re}_\lambda \leqslant 399$, for a resolution of $k_{\max}\eta \approx 2.0$, where $k_{\max}$ is the maximum resolved wave number and η is the Kolmogorov microscale. Most of the IVS characteristics are confirmed at the higher Reynolds numbers analyzed in this work; e.g., the results confirm that the mean radius of the IVS $\langle R_{ivs}\rangle$ is approximately equal to $\langle R_{ivs}\rangle/\eta \approx 4$–5 and that the mean radius is equal to the radius of the stationary Burgers vortex $\langle R_{ivs}/R_B\rangle \approx 1.0$, with $R_B = 2(\nu/\alpha)^{1/2}$, where ν is the kinematic viscosity and α is the (locally) imposed rate of strain. Moreover, the tangential velocity of the IVS scales with the root-mean-square velocity of the flow $U_{ivs} \sim u'$. These IVS characteristics seem to be robust and relatively independent of the Reynolds number; however, there are other quantities for which the classical results do not hold. A notable example is the mean length of the IVS $\langle L_{ivs}\rangle$, which previous works, carried out at smaller Reynolds numbers, claimed to scale with either the Taylor microscale λ or the integral scale of turbulence L. It turns out that the correct scaling for this quantity can be observed only at $\mathrm{Re}_\lambda \gtrsim 200$, and the results consistently show that L_{ivs} scales with the Kolmogorov microscale $L_{ivs} \sim \eta$, with a mean value equal to $\langle L_{ivs}\rangle \approx 60\eta$. The present findings provide further evidence that $\mathrm{Re}_\lambda \gtrsim 200$ is required for the small scales to be fully developed.

DOI: 10.1103/PhysRevFluids.7.104605

I. INTRODUCTION

One of the most distinctive characteristics of turbulent flows is the presence of a large range of eddy structures, defined loosely as regions of concentrated vorticity and low pressure, with a life time which is usually big compared with the characteristic timescale of the flow [1,2]. These coherent vorticity structures have been studied for many years since they are related to the viscous dissipation mechanism and to the internal intermittency [3]. Their study is also motivated by their role on transport, mixing, and diffusing at the small scales of motion within the flow [4,5].

To identify vortical structures, several methods can be employed as discussed in [4,6]. The use of isosurfaces of vorticity has been widely used in homogeneous and isotropic turbulence and was the method used by those who first brought these structures to the attention, e.g., [7–10]. Other tracking methods have been used in channel flows and mixing layers, [11,12]. Along with the vorticity magnitude, an analysis through velocity gradient invariants has been used to infer the flow

---

[*] carlos.silva@tecnico.ulisboa.pt

TABLE I. Statistics of the intense vorticity structures (IVS) as obtained in several flows: Forced Isotropic Turbulence (FHIT), Decaying Isotropic Turbulence (DHIT), Homogeneous Shear (HS), Mixing Layer (ML), Circular Duct Flow (DF), Boundary Layer Flow (BL), Channel Flow (CF), Round Jet (RJ), Plane Jet (PL), and Free Shear Flow (FSF). Taylor-based Reynolds number Re_λ; mean radius of IVS $\langle R_{ivs}\rangle$ normalized by the Kolmogorov microscale η; mean value of the IVS radius normalized by the local Burgers radius $\langle R_{ivs}/R_B\rangle$; mean value of the azimuthal velocity $\langle U_{ivs}\rangle$ normalized by the root-mean-square velocity u'; mean value of the azimuthal velocity $\langle U_{ivs}\rangle$ normalized by the Kolmogorov velocity u_η; mean value of the length of the IVS $\langle L_{ivs}\rangle$ normalized by the integral length scale L; mean value of the length of the IVS $\langle L_{ivs}\rangle$ normalized by the Kolmogorov microscale η. The Reynolds numbers Re_λ in [11] were estimated with the available data in the paper. In [5,20] the reference values λ, u', and η are taken from the conditional mean profiles for each instantaneous field, which are roughly constant deep inside the turbulent region.

Flow	Ref.	Re_λ	$\langle R_{ivs}\rangle/\eta$	$\langle R_{ivs}/R_B\rangle$	$\langle U_{ivs}\rangle/u'$	$\langle U_{ivs}\rangle/u_\eta$	$\langle L_{ivs}\rangle/L$	$\langle L_{ivs}\rangle/\eta$
FHIT	[13]	36–168	3.8–4.2	–	–	–	16.5–21.1	94.80–570.24
FHIT	[14]	37–168	4.8–4.9	0.92–1.05	0.86–0.99	–	–	58.6–310.9
FHIT	[4]	46	3.2–3.8	–	–	–	14.7–32.4	–
FHIT	[5]	111	4.6	0.99	0.68	9.0	28.8	–
DHIT	[14]	62	4.8	0.82	1.21	–	–	184.0
HS	[4]	–	4.9–5.2	–	–	–	–	–
ML	[12]	80–100	4.5	–	0.50	–	–	–
DF	[19]	719–1934	5.5–6.2	1	0.59–0.64	8.7–14.0	10.5–12.3	–
BL	[19]	332–1304	5.2–6.2	1	0.68–0.82	7.6–12.8	13.6–13.7	–
CF	[11]	200–380	4.0–5.0	–	–	1.2–2.0	–	–
RJ	[18]	150	3.0–7.5	–	–	–	–	–
PJ	[5]	120	4.6	0.97	0.76	7.15	28.3	–
FSF	[20]	115	4.5	1.0	–	–	–	–

topology [4,11,12], namely, to distinguish between swirling tubular vortices (tubelike structures) and shear flat vortices (sheetlike structures), which appear simultaneously in high-vorticity regions with strong background/mean shear [11,12].

Among these structures are the so-called intense vorticity structures (IVS). The IVS constitute the smallest scale eddies that can be found in the flow, in terms of their vortex core sizes, with a particularly intense local vorticity, while the associated kinetic energy content and contribution to the total dissipation are both negligible [13,14]. At the same time the life times of these structures is quite large (on the order of the integral timescale of the flow) [2].

Topologically they are characterized by swirling slender tubular vortices, which is the reason why they are often referred to as “worms.” These structures are identified by means of a vorticity magnitude threshold ω_{ivs}. Jiménez *et al.* [13] defined this as the vorticity magnitude above which the flow points with the highest enstrophy represent 1% of the total [13,14]. The features of these structures have been investigated by many researchers using DNS of isotropic turbulence, e.g., [7–10,13–17]. Experimental studies addressing these structures in (approximately) isotropic turbulence include, e.g., [2,6,18].

These IVS have also been studied in other types of flows such as mixing layers [12], channel flows [11], and jets [5,18]. So far, similar statistics have been presented for these types of structures independently of the nature of the flow considered. For instance, it has been observed that the radius of the IVS is $\langle R_{ivs}\rangle \approx 4\eta$–$5\eta$ in isotropic turbulence [13,14], mixing layers [12], channel flow [11], and jets [5,18], where η is the Kolmogorov microscale. These results have been achieved in spite of the different tracking methods used [5], as can be seen when comparing, e.g., [11,13].

Table I lists the mean values of several of the IVS characteristics computed or estimated in different flow types. The mean radius of the IVS has been observed to be close to the Kolmogorov microscale $\langle R_{ivs}\rangle/\eta \approx 4-5$, while the mean tangential velocity is close to the root-mean-square

TABLE II. Physical and computational parameters of the DNS: Number of colocation points (N^3); Taylor microscale-based Reynolds number (Re_λ); kinematic viscosity (ν); root mean square of the velocity fluctuations ($u' = \sqrt{\overline{u(\vec{x},t)^2}}$); Taylor microscale ($\lambda$); integral length scale (L); viscous dissipation rate (ε); Kolmogorov microscale (η); maximum effective wave number normalized by the Kolmogorov microscale ($k_{\max}\eta$); number of instantaneous fields used in the subsequent analysis (N_f). The computation of these quantities is described in Appendix A.

N^3	Re_λ	ν	u'	λ	L	ε	η	$k_{\max}\eta$	N_f
256^3	90	0.0145	2.97	0.44	0.90	9.98	0.0235	2.0	71
512^3	148	0.0057	2.98	0.28	0.84	9.54	0.0118	2.0	8
768^3	191	0.0034	3.01	0.22	0.86	9.88	0.0079	2.0	4
1024^3	242	0.0023	3.04	0.18	0.84	9.52	0.0060	2.0	1
1536^3	314	0.0014	3.06	0.14	0.86	9.84	0.0040	2.0	1
2048^3	292	0.0009	2.68	0.10	0.60	10.07	0.0029	2.0	1
2048^3	399	0.0010	3.35	0.12	0.96	11.91	0.0030	2.1	1

velocity $\langle U_{ivs}\rangle/u' \approx 1$. The values for the mean length of the "worms" show more variability, but it has been argued that it scales with the integral scale of turbulence [13,14]. Other authors have suggested that it scales with the Taylor microscale instead, e.g., [6,21,22]. Furthermore, Jiménez and Wray [14] found evidence for integral and for Taylor scaling depending on the definition used for the IVS length. Notice that the values in Table I corresponding to the highest Reynolds numbers have been estimated, and not directly computed. To the authors' knowledge, the higher value of the Reynolds number presently available for computed IVS characteristics is still $\mathrm{Re}_\lambda = 168$ used in [13,14].

Because many of the classical results concerning these structures have been obtained with low to moderate Reynolds numbers, and because it has recently become clear that for some problems the asymptotic scaling laws can only be observed for Reynolds numbers based on the Taylor microscale above at least $\mathrm{Re}_\lambda \gtrsim 200$ (e.g., see [23–25]), the present work revisits these results by using state-of-the-art direct numerical simulations (DNS) of isotropic turbulence carried out at moderate to high Reynolds numbers.

This paper is organized as follows. Section II describes the DNS used in the present work. Section III describes the method employed to compute the IVS characteristics, and Sec. IV analyzes the results obtained. The work ends in Sec. V with an overview of the main results and conclusions.

II. DIRECT NUMERICAL SIMULATIONS OF FORCED HIT

A total of seven DNS of statistically stationary (forced) homogeneous isotropic turbulence (FHIT) are used in the present work, where the forcing is the one described in Alvelius [26]. The code used for these simulations has been used extensively in other works (see, e.g., [24] and references therein), and Table II lists all the physical and computational parameters of these simulations. Details of this code including the computation of the quantities listed in Table II and of the forcing scheme are given in Appendix A.

The number of collocation points in the simulations varies in the range $256 \leqslant N^3 \leqslant 2048^3$ and the Reynolds number in the range $90 \leqslant \mathrm{Re}_\lambda \leqslant 399$, while the resolution is always kept at $k_{\max}\eta \geqslant 2.0$. Statistical stationarity is obtained by applying a power input through the imposed forcing [26] that balances the viscous dissipation rate (on average) $P = \varepsilon$, and all the present simulations use the same power of the input forcing, $P = 10$ (see Appendix A for more details).

In all simulations the longitudinal integral scale $L \approx 0.85$ is indirectly imposed through the forcing, which is concentrated in the first two wave numbers centered at $k_p = 2$, except for the simulation with $\mathrm{Re}_\lambda = 292$, where the forcing is imposed in the first four wave numbers centered at

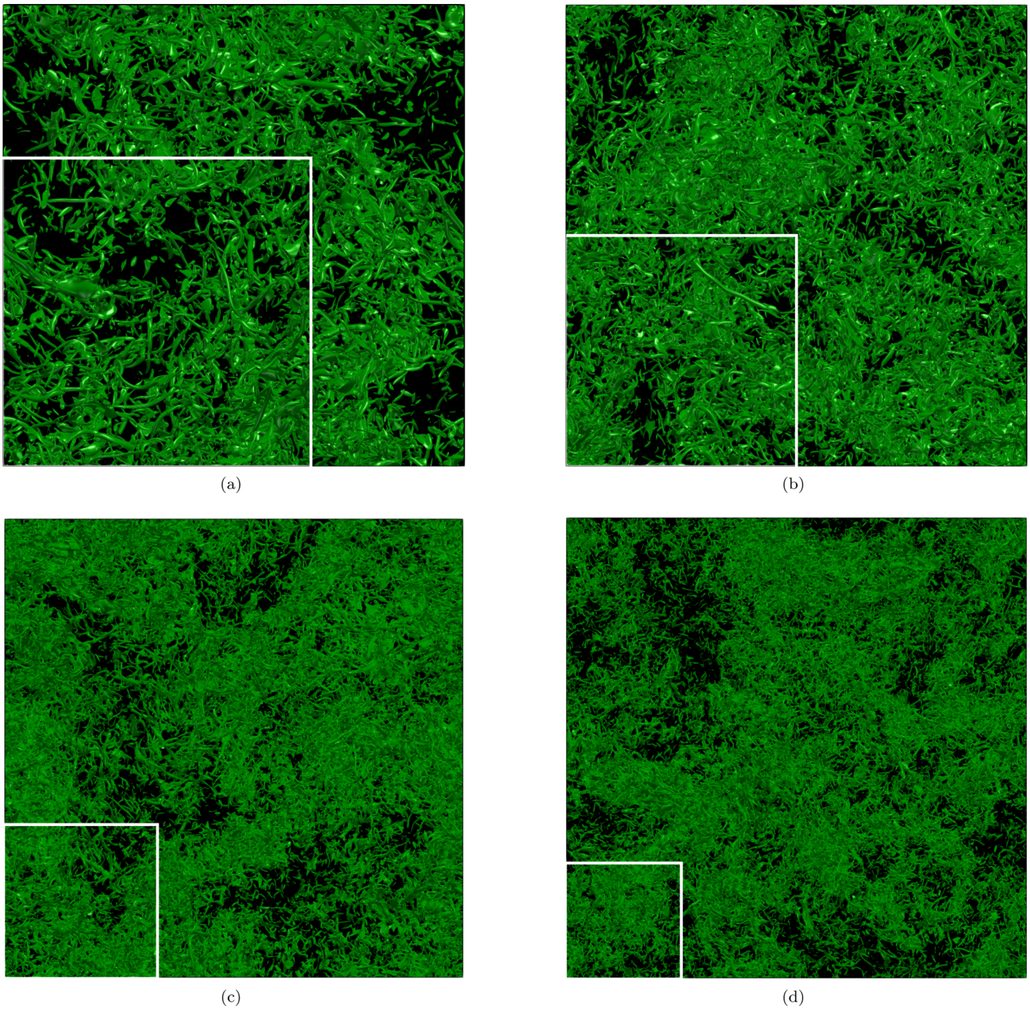

(a) (b) (c) (d)

FIG. 1. Isosurfaces of vorticity magnitude corresponding to the volume occupied by the 1% most intense vorticity showing the computation domain for the DNS with (a) $N^3 = 768^3$ ($\mathrm{Re}_\lambda = 191$); (b) $N^3 = 1024^3$ ($\mathrm{Re}_\lambda = 242$); (c) $N^3 = 1536^3$ ($\mathrm{Re}_\lambda = 314$); and (d) $N^3 = 2048^3$ ($\mathrm{Re}_\lambda = 399$). Notice that whereas in (a) and (b) the entire computational box is shown, in (c) and (d) only 1024 grid points in the direction perpendicular to the plane of the figure are used. The white squares at the bottom-left corners of each panel show a subregion of the flow domain used later (Fig. 12).

$k_p = 4$. This simulation was carried out specifically to assess the influence of the size of the integral scale. Thus, in all cases the integral scale of turbulence is always more than seven times smaller than the size of the computational box in order to prevent confinement effects (see Table II).

The subsequent analysis uses several instantaneous fields from each of the DNS of FHIT, and in order to provide a similar level of convergence in the results from the different cases a larger number of instantaneous fields N_f has been used for the simulations with a smaller number of collocation points. Thus, all the statistics were computed using only these instantaneous fields; e.g., four instantaneous fields were used to compute all the statistics (in Table II) and IVS characteristics of the simulation with $N^3 = 768^3$ colocation points ($\mathrm{Re}_\lambda = 191$).

Figure 1 shows isosurfaces of vorticity magnitude $\sqrt{\omega_i \omega_i}$, where $\omega_i = \varepsilon_{ijk} \partial u_i / \partial x_j$ is the vorticity vector (ε_{ijk} is the permutation tensor), displaying the entire computational domain for the

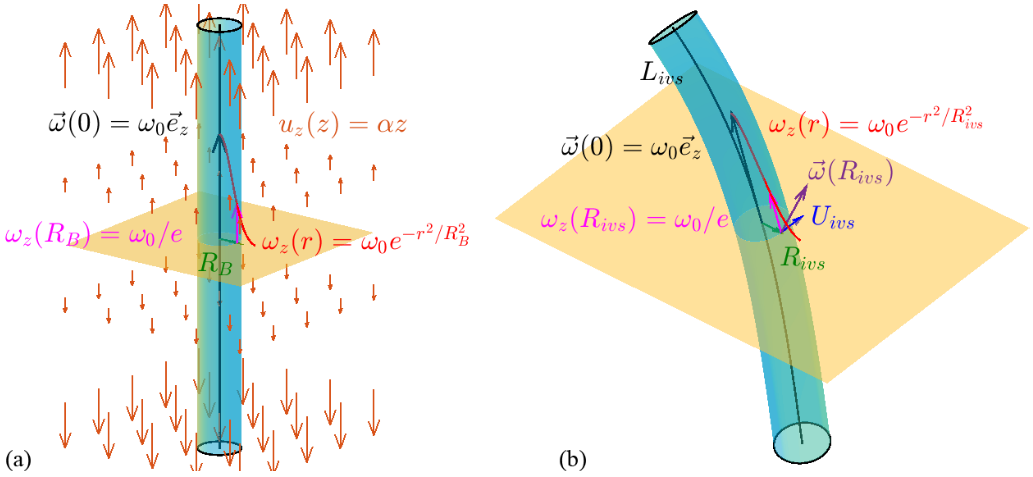

FIG. 2. (a) Sketch of the Burgers vortex model created by a field of uniform axial velocity $u_z = \alpha z$. The radial profile of the axial vorticity is given by $\omega_z(r) = \omega_0 e^{-r^2/R_B^2}$, where ω_0 is the maximum vorticity, and the vortex core radius (defined as the Burgers radius) is obtained through $\omega(r = R_B) = \omega_0/e$. (b) Sketch of a detected IVS indicating the local tangential velocity U_{ivs}, local core radius R_{ivs}, and its length L_{ivs}, computed along the axis center, defined by following the direction of the maximum local vorticity.

simulations with $768^3 \leqslant N^3 \leqslant 2048^3$ collocation points and $191 \leqslant \mathrm{Re}_\lambda \leqslant 399$. The vorticity magnitude threshold used in the figures corresponds to particularly intense vorticity. Specifically, the vorticity magnitude corresponds to 1% of the volume occupied by the most intense vorticity events. These IVS or "worms" will be investigated in the present work, and it is clear that they exhibit a tubular shape with a mild curvature which is characteristic of the regions of intense vorticity observed in DNS of numerous flow configurations, e.g., [3,10,13,14] and many others.

III. DETERMINATION OF THE LOCAL CHARACTERISTICS OF THE INTENSE VORTICITY STRUCTURES

A. The Burgers vortex model

It has been shown in several works, e.g., [11,13,14], that the IVS are well represented by a classical Burgers vortex model for describing the radial vorticity profile and the radii of the IVS (see the discussion in Sec. IV A). Figure 2(a) shows a sketch of the Burgers vortex model which consists of a steady and axisymmetric vortex tube subjected to a stretching strain field oriented along its vorticity vector. Note that the compressive radial strain is not included in this figure for simplicity.

Using cylindrical coordinates and writing the imposed axial (z) component of the velocity field as

$$u_z(z) = \alpha z, \tag{1}$$

where α is the rate of strain, a solution of the Navier-Stokes equations is readily obtained in which the radial (r) and tangential (θ) velocity components are given by

$$u_r(r) = -\tfrac{1}{2}\alpha r \tag{2}$$

and

$$u_\theta(r) = \frac{\Gamma}{2\pi r}\left(1 - e^{-r^2/R_B^2}\right), \tag{3}$$

respectively, where Γ is the circulation computed with the axial vorticity $\omega_z(r)$,

$$\Gamma = 2\pi \int_0^\infty \omega_z(r) r dr, \tag{4}$$

and R_B is the Burgers radius,

$$R_B = 2\left(\frac{\nu}{\alpha}\right)^{1/2}. \tag{5}$$

From these equations it follows that the radial profile of the axial vorticity for a steady Burgers vortex is given by

$$\omega_z(r) = \frac{\alpha\Gamma}{4\pi\nu} e^{-r^2/R_B^2}, \tag{6}$$

while the other vorticity components are zero, $\omega_r = \omega_\theta = 0$.

B. The WORMTRACKER algorithm

As described in the introduction and following [13,14], the IVS are defined as flow points with the highest vorticity magnitude covering 1% of the total flow domain. In order to implement this definition an histogram of vorticity magnitude is computed for each instantaneous field of each simulation (N_f) in order to obtain the reference vorticity magnitude threshold ω_{ivs} which separates the flow points into two regions: points pertaining to the IVS are defined by having a local vorticity magnitude ω obeying the relation $\omega > \omega_{ivs}$. After this, flow points with $\omega > \omega_{ivs}$ are assigned to individual IVS.

The present work uses a numerical code originally developed by da Silva *et al.* [5], which has many similarities with the algorithm described by Jiménez *et al.* [13,14], with some differences: (1) for each axis point of each IVS the tangential velocity is directly computed by interpolating the velocity field into a plane that is normal to the local axis [see Fig. 2(b)] and (2) the length of each detected IVS is directly computed using the vorticity magnitude threshold used to define the IVS, by adding the successive points along the axis. Moreover, several modifications were recently implemented to the present code, in relation to the version used in da Silva *et al.* [5], in order to allow the processing of very large data banks used in here. More details are described in Appendix B.

The present WORMTRACKER algorithm starts by identifying the points on the axis of each structure corresponding the maximum value of local vorticity magnitude. Once a point along the axis of a worm has been detected the local vortex radius for each IVS is computed by assuming that the local radial vorticity profile is Gaussian, i.e.,

$$\omega_z(r) = \omega_0 e^{-r^2/R_{ivs}^2}, \tag{7}$$

where ω_0 is the axial vorticity located at the axis, r is the radial coordinate normal to the axis, and R_{ivs} is the local radius of the identified worm. Note that this approximation, i.e., a Gaussian radial vorticity profile, is totally consistent with the Burgers vortex model described in Eq. (6). Based on this equation the WORMTRACKER algorithm computes the local vortex radius as the radial distance (measured from the IVS axis) where the azimuthal average of the local axial vorticity is equal to

$$\omega_z(r = R_{ivs}) = \omega_0/e. \tag{8}$$

Then the (local) characteristic circulation of each worm at any axial position is

$$\Gamma = 2\pi \langle U_{ivs}\rangle_\theta R_{ivs}, \tag{9}$$

where $\langle\,\rangle_\theta$ represents an azimuthal average, while the worm circulation-based Reynolds number is defined by

$$\mathrm{Re}_\Gamma = \frac{\Gamma_{ivs}}{\nu}, \tag{10}$$

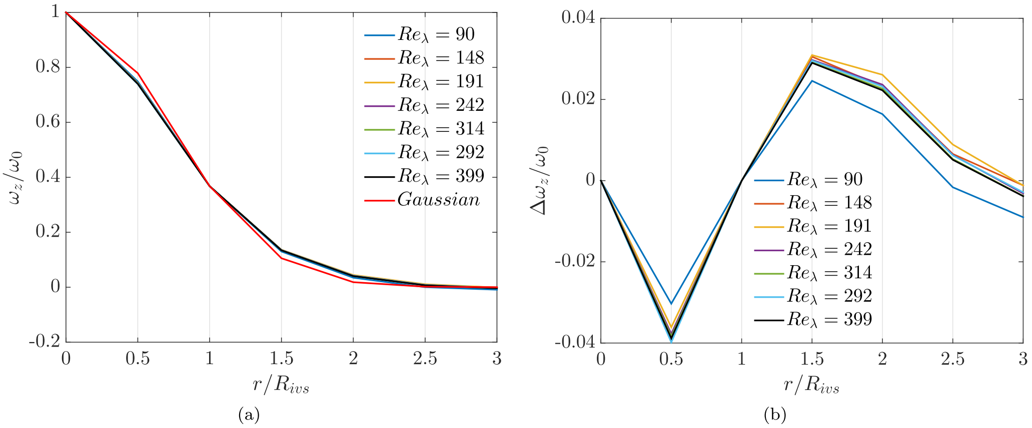

FIG. 3. (a) Mean (radial) profiles of axial vorticity $\omega_z(r)$ obtained through an azimuthal and axial average, carried out for each detected "worm" for all the DNS used in the present work, compared to a Gaussian profile defined in Eq. (7). The radial profiles are normalized with the radius of the intense vorticity structures R_{ivs} and centerline axial vorticity ω_0. (b) Mean error $\Delta\omega_z$, between the Gaussian profile described in Eq. (7) and the mean (radial) profiles of axial vorticity $\omega_z(r)$.

where Γ_{ivs} is the circulation of a given individual "worm." In Eq. (9) U_{ivs} is the (local) tangential velocity which is computed directly from the local velocity field projected into a plane perpendicular to the local vorticity on the axis [see Fig. 2(b)]. Specifically, for each detected axis point, the three-dimensional velocity field $\vec{u}(\vec{x},t)$ is first projected into the plane defined by the local vorticity at this axis [see Fig. 2(b)]. After this, the (2D) velocity vector field in this plane is decomposed into cylindrical coordinates at $r = R_{ivs}$ (using as origin/center the local axis of the IVS), with different tangential velocities for several azimuthal angles θ_i around the axis of the IVS, i.e., $u_\theta(r = R_{ivs}, \theta_i)$. Finally, the local tangential velocity is the azimuthal average over all those angles, $U_{ivs} = \sum u_\theta(r = R_{ivs}, \theta_i)/N_\theta$ (see Appendix B for more details). The advection velocity of each of the IVS is not subtracted from the instantaneous velocity. This is different from the approach used in, e.g., [13,14] where the computation of U_{ivs} is based on the Gaussian (approximation) vorticity profile described in Eq. (7), leading to $U_{ivs} = 0.319\omega_0 R_{ivs}$ which is not used here. Finally, the length of each worm L_{ivs} is computed by measuring the length of each detected filament along its axis, defined by the selected vorticity magnitude threshold, ω_{ivs}. Specifically, for each "worm" or IVS axis, the total length L_{ivs} is computed by adding together the individual segments of the structure, $L_{ivs} = \sum dL_{ivs}$, where dL_{ivs} is the distance between two nearby axis points, and the sum is done from the start to the end of the "worm" structure, whose limits are again defined with the selected vorticity magnitude threshold, ω_{ivs}.

Once an axis point has been detected the direction of the local vorticity vector at this point determines the next (neighboring) axis point. Specifically, since all the axis points of the IVS are located at coordinates of the computational grid, the direction of the local vorticity vector at a particular axis point suggests four possible "candidate points" from the adjacent plane of the computational grid. The selected "candidate" for new axis point is the one with the highest vorticity magnitude, provided this point has not yet been selected as belonging to (another) previously identified "worm."

As in [13] the assumption of a Gaussian radial vorticity profile, which is used here to compute the local worm radius R_{ivs} through Eq. (8), was tested using results from the present DNS. Figure 3(a) compares the Gaussian mean radial profiles of axial vorticity $\omega_z(r)$ given by Eq. (7) with the profiles obtained by making an azimuthal average of the axial vorticity followed by an axial average over all the axial points of each of the detected worms, for all the present DNS. Figure 3(b) shows the mean error between these two curves. As can be seen the error is quite small, with less than 4% maximum

TABLE III. Mean values of the characteristics of intense vorticity structures (IVS) for the several simulations used in the present work (described in Table II): number of colocation points (N^3); Taylor microscale-based Reynolds number (Re_λ); mean radius normalized by the Kolmogorov microscale ($\langle R_{ivs}\rangle/\eta$); mean radius normalized by the local Burgers radius ($\langle R_{ivs}/R_B\rangle$); mean radius normalized by the Taylor microscale ($\langle R_{ivs}\rangle/\lambda$); mean value of the tangential velocity normalized by the Kolmogorov velocity ($\langle U_{ivs}\rangle/u_\eta$); mean value of the tangential velocity normalized by the root-mean-square velocity ($\langle U_{ivs}\rangle/u'$); mean length normalized by the longitudinal integral scale ($\langle L_{ivs}\rangle/L$); mean length normalized by the Kolmogorov microscale ($\langle L_{ivs}\rangle/\eta$); mean length normalized by the Taylor microscale ($\langle L_{ivs}\rangle/\lambda$); mean value of the axial vorticity normalized by the root-mean-square vorticity and Taylor-based Reynolds number ($\langle\omega_{ivs}\rangle\mathrm{Re}_\lambda^{-1/2}/\omega'$); mean value of the circulation Reynolds number normalized by the Taylor-based Reynolds number ($\langle\mathrm{Re}_\Gamma\rangle\mathrm{Re}_\lambda^{-1/2}$).

N^3	Re_λ	$\frac{\langle R_{ivs}\rangle}{\eta}$	$\langle\frac{R_{ivs}}{R_B}\rangle$	$\frac{\langle R_{ivs}\rangle}{\lambda}$	$\frac{\langle U_{ivs}\rangle}{u_\eta}$	$\frac{\langle U_{ivs}\rangle}{u'}$	$\frac{\langle L_{ivs}\rangle}{L}$	$\frac{\langle L_{ivs}\rangle}{\eta}$	$\frac{\langle L_{ivs}\rangle}{\lambda}$	$\frac{\langle\omega_{ivs}\rangle}{\omega'\mathrm{Re}_\lambda^{1/2}}$	$\frac{\langle\mathrm{Re}_\Gamma\rangle}{\mathrm{Re}_\lambda^{1/2}}$
256^3	90	4.28	0.96	0.23	6.01	1.25	1.27	48.70	2.61	0.41	14.36
512^3	148	4.23	0.98	0.18	7.11	1.15	0.75	53.18	2.22	0.35	13.01
768^3	191	4.10	0.97	0.15	7.83	1.11	0.51	54.98	2.02	0.32	12.19
1024^3	242	4.06	0.98	0.13	8.31	1.05	0.40	55.86	1.82	0.29	11.32
1536^3	314	3.98	0.98	0.11	9.33	1.04	0.26	56.56	1.62	0.27	10.92
2048^3	292	3.98	0.98	0.12	9.37	1.08	0.28	57.81	1.72	0.28	11.34
2048^3	399	3.90	0.97	0.10	10.23	1.01	0.18	55.90	1.42	0.24	10.35

error [Fig. 3(a) is remarkably similar to Fig. 1(b) in [14]]. To summarize, as in [13] the Gaussian approximation agrees very well with the present data, which validates its use in the present work.

IV. THE CHARACTERISTICS OF THE INTENSE VORTICITY STRUCTURES AT HIGH REYNOLDS NUMBERS

In this section we analyze the characteristics of the intense vorticity structures computed with the algorithm described in Sec. III, using the DNS described in Sec. II. The mean values of the several quantities obtained for the IVS are listed in Table III.

A. The radius of the intense vorticity structures

We start by analyzing the mean radius of the "worms" as shown in Figs. 4(a) and 4(b). For each simulation the local radius of each IVS, R_{ivs}, is computed at each point of the local axis by using Eq. (8). In agreement with many previous works (compare also the values in Tables I and III) the mean radius of the IVS is of $\langle R_{ivs}\rangle/\eta \approx 4$, independent of the Reynolds number [see Fig. 4(a)]. This well-known result is confirmed here for the highest Reynolds numbers available in the present work, which are much bigger than previously available (existing DNS with even higher Reynolds numbers are described in, e.g., [27–29]; however, the IVS properties were not analyzed in those simulations). As described in [1,13] this fact merely results from the fact that the stretching rate acting upon the IVS is $\alpha \sim \omega'$, which from Eq. (5) leads to $R_B \sim \eta$, since the IVS are well described by a stable Burgers vortex (a Taylor scaling would imply that the stretching acting on the IVS is caused by the large-scale strain $\alpha \sim u'/L$). An anonymous referee remarked, however, that the length of the IVS is not consistent with a Burgers vortex model since the intense strain is not coherent over very long distances. Indeed, the IVS emerge from a nonlinear process that cannot be described by the simple (linear) Burgers vortex model.

As described in the previous section the algorithm used here to track the IVS relies on the Burgers vortex model, and it is important to again check whether this model does indeed represent a typical IVS, for all of the range of Reynolds numbers available. Already while discussing Fig. 3 it was noted that the azimuthally averaged radial vorticity profiles of the IVS are approximately Gaussian, which is consistent with the Burgers model as described in Eq. (6). However, it is important to check

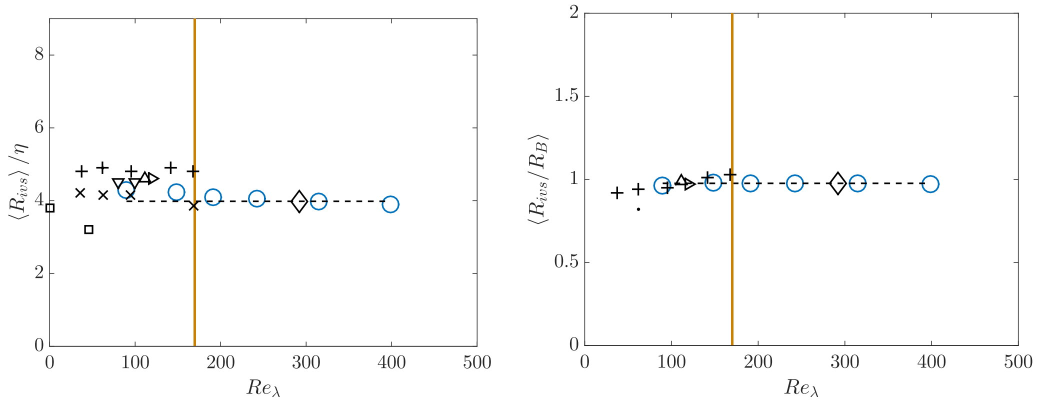

(a)

(b)

FIG. 4. Mean radius of the intense vorticity structures normalized by the (a) Kolmogorov microscale $\langle R_{ivs}\rangle/\eta$ and (b) local Burgers radius $\langle R_{ivs}/R_B\rangle$ as function of the Reynolds number Re_λ, for all the simulations carried out in the present work (blue circles), compared to results obtained in the literature: Jiménez *et al.* [13] ($\times$), Jiménez and Wray [14] ($+$), Jiménez and Wray [14] ($\cdot$) (DHIT), Kida and Miura [4] ($\square$), Silva *et al.* [5] ($\triangle$), Tanahashi *et al.* [12] ($\triangledown$), and Silva *et al.* [5] ($\triangleright$) (PJ). The black diamond represents the simulation with a smaller integral scale ($\mathrm{Re}_\lambda = 292$), and the vertical orange line represents the highest Reynolds number previously available in the literature [14].

whether the local IVS radius is consistent (as predicted in the Burgers vortex model) with the local stretching rate measured at each IVS.

In order to assess this, the local strain rate α acting at each of the IVS was evaluated by computing the local stretching rate at each axial point for each IVS, i.e., $\alpha = \omega_i\omega_j S_{ij}/\omega^2$. The local Burgers radius was then computed at each axis point (for each IVS) using Eq. (5), and it was then compared with the measured local radius, computed as described in Sec. III A.

The results from Fig. 4(b) show the mean radius normalized by the local Burgers radius, with $\langle R_{ivs}/R_B\rangle \approx 1.0$ for all the simulations used in the present work. Clearly, the mean radius of the IVS scales with the Burgers radius for relatively small Reynolds numbers as well as for the higher Reynolds number cases, which are much higher than previously available. This again confirms that also at the much higher Reynolds numbers available in the present work the IVS are well modeled by equilibrium Burgers vortices [13,14].

The probability density functions (PDFs) for R_{ivs}/η and R_{ivs}/R_B are shown in Fig. 5 and essentially confirm in more detail the main conclusions already discussed in relation to Figs. 4(a) and 4(b). These PDFs are very similar to the ones shown in, e.g., [13,14] in isotropic turbulence and in [11,12] in other (inhomogeneous) flow types. They show that the most probable local radius of the "worms" is $R_{ivs}/\eta \approx 4$ and $R_{ivs}/R_B \approx 1$, again confirming the fact that the typical IVS are well represented by a steady Burgers vortex model. It is also interesting to observe that, contrary to Figs. 4(a) and 4(b), the Reynolds number does have a mild influence in the shape of the curves. Specifically, as the Reynolds number increases, the probability of finding IVS with smaller local radius increases [see the left tail of the PDF for $R_{ivs}/\eta \approx 1$; Fig. 5(a)]. Specifically, Fig. 5(a) shows that the smallest R_{ivs} do not collapse in Kolmogorov scaling (see also [14]). These "thin" IVS are associated with extreme velocity gradients, which reveal anomalous scaling behavior. Indeed, different scaling laws have been proposed to capture their decreasing size with increasing Reynolds number [14,28,30].

Interestingly the Reynolds number has virtually no effect on the PDF of R_{ivs}/R_B for small local radius $R_{ivs}/R_B < 1$; however, the same is not true for high local radius $R_{ivs}/R_B > 1$ where, as the Reynolds number increases, the probability of finding IVS with higher local radius (normalized by the local Burgers radius) increases [see Fig. 5(b)]. Also, it is clear that the shape of the PDFs

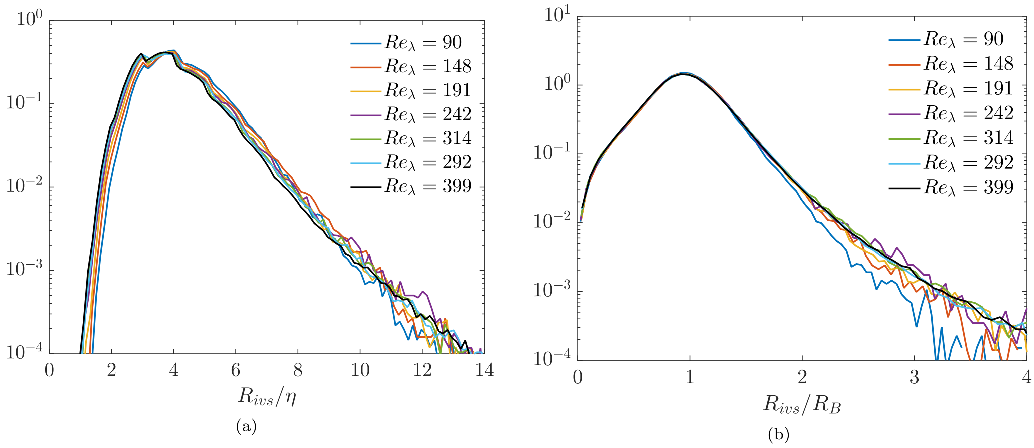

(a)

(b)

FIG. 5. Probability density functions (PDFs) of the local radius R_{ivs} of the intense vorticity structures for all the simulations carried out in the present work normalized by (a) the Kolmogorov microscale η and (b) the local Burgers radius R_B.

of R_{ivs}/R_B converges only to the final PDF [that for higher Reynolds number, $\mathrm{Re}_\lambda = 242$ ($N^3 = 1024^3$)] for $\mathrm{Re}_\lambda \gtrsim 200$.

An even stronger demonstration of the robustness of the Burgers vortex model to describe the characteristics of the IVS can be gained by looking at Fig. 6 showing joint probability density functions (JPDFs) of the local radius R_{ivs} and stretching rate α for all the simulations carried out in the present work. A similar plot has been presented in [14]. It is clear that higher values of the stretching rate are associated with smaller values of the local radius, and conversely, smaller values

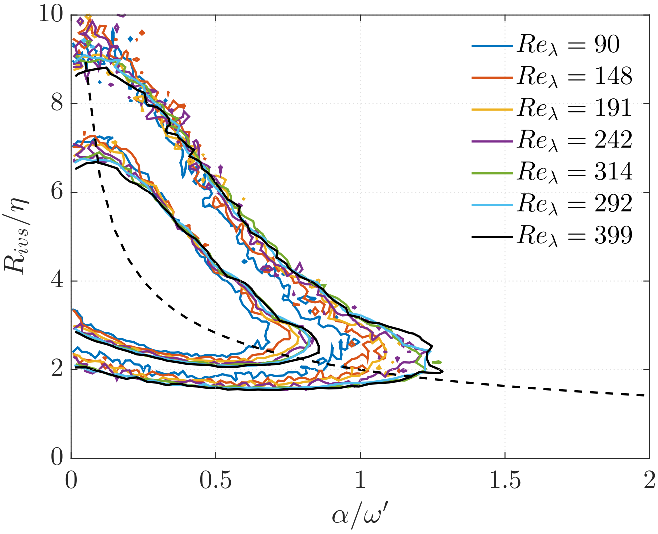

FIG. 6. Joint probability density functions (JPDFs) of local radius normalized by the Kolmogorov microscale R_{ivs}/η and stretching rate normalized by the root-mean-square vorticity α/ω' for all the simulations carried out in the present work (only stretching events $\alpha > 0$ are represented). The dashed line in Fig. 6 corresponds to the Burgers radius, $R_B/\eta = 2(\alpha/\omega')^{-1/2}$ from Eq. (5). Each simulation (or Reynolds number case) is assessed with two contour values equal to 0.1 and 0.01, respectively.

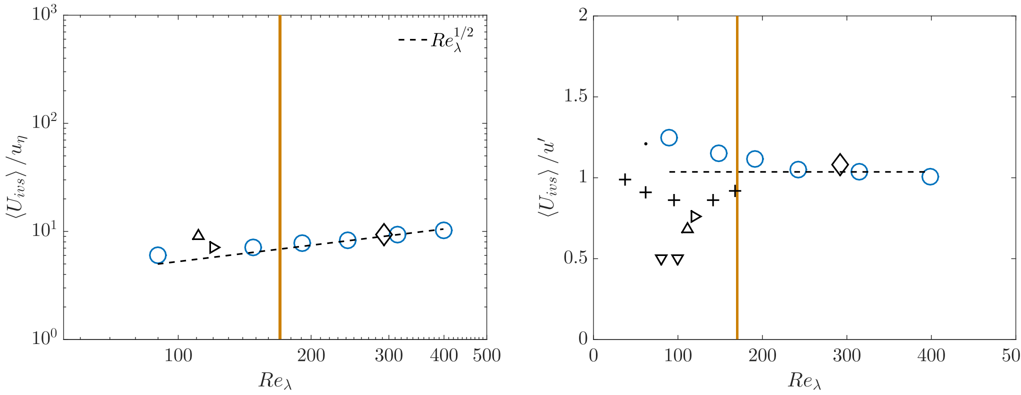

(a) (b)

FIG. 7. Mean tangential velocity of the intense vorticity structures normalized by the (a) Kolmogorov velocity $\langle U_{ivs}\rangle/u_\eta$ and (b) root-mean-square velocity $\langle U_{ivs}\rangle/u'$ as function of the Reynolds number Re_λ, for all the simulations carried out in the present work (blue circles), compared to results obtained in the literature: Jiménez *et al.* [13] ($\times$), Jiménez and Wray [14] ($+$), Jiménez and Wray [14] ($\cdot$) (DHIT), Silva *et al.* [5] ($\triangle$), Tanahashi *et al.* [12] ($\triangledown$), and Silva *et al.* [5] ($\triangleright$) (PJ). The black diamond represents the simulation with a smaller integral scale ($\mathrm{Re}_\lambda = 292$), and the vertical orange lines represent the highest Reynolds number previously available in the literature [14].

of the stretching rate lead to fatter local IVS, as expected in a Burgers vortex. The dashed line in Fig. 6 corresponds to the Burgers radius; i.e., the relation described in Eq. (5) and the JPDFs are clearly aligned with this dashed line, again confirming the Burgers vortex model assumption for all the present simulations, independently of the Reynolds number. Interestingly, this figure shows also that as the Reynolds number increases the local stretching rates existing within the flow also increase, and this is concomitant with a smaller associated local radius (see Fig. 6 near $\alpha/\omega' \gtrsim 1$ and $2 \lesssim R_{ivs}/\eta \lesssim 3$). Also, for a given small value of the stretching rate the increase of the Reynolds number decreases the local vortex radius, as expected directly from the definition of the Burgers vortex radius (see Fig. 6 near $\alpha/\omega' \approx 0.2$ and $9 \lesssim R_{ivs}/\eta \lesssim 10$).

To conclude, the analysis of the radius of the IVS shows that these structures display a characteristic radius of $\langle R_{ivs}\rangle/\eta \approx 4$ and $\langle R_{ivs}/R_B\rangle \approx 1$, independently of the Reynolds number for the range of Reynolds numbers considered in the present work. The effects of the (increase) of the Reynolds number can only be felt at the extreme, low-probability, events of these variables, but even in these cases the robustness of the Burgers vortex model is clearly apparent.

B. The tangential velocity of the intense vorticity structures

The tangential velocity of the IVS, U_{ivs}, as defined in Sec. III B, is analyzed next. As described in Sec. III B the (local) tangential velocity for each IVS is directly computed by projecting the local velocity field into a plane perpendicular to the vorticity vector identifying this particular structure. It has been advanced that this velocity scales with the root-mean- square velocity, $\langle U_{ivs}\rangle \sim u'$ [12,13], and the goal of the present section is to assess whether this is the case here, for all the Reynolds numbers considered in the present work, which are much higher than previously available in these studies.

Figure 7 shows the mean values of the tangential velocity of the IVS [Fig. 7(a)] normalized by the Kolmogorov velocity $\langle U_{ivs}\rangle/u_\eta$ and [Fig. 7(b)] by the root-mean-square velocity $\langle U_{ivs}\rangle/u'$. The plots confirm that indeed the mean tangential velocity of the IVS scales with the root-mean-square velocity, as described in [13,14] and as confirmed in numerous other works, e.g., [12]. In particular we obtain $\langle U_{ivs}\rangle/u' \approx 1.0$ in agreement with many previous results (see Table I). The scaling law

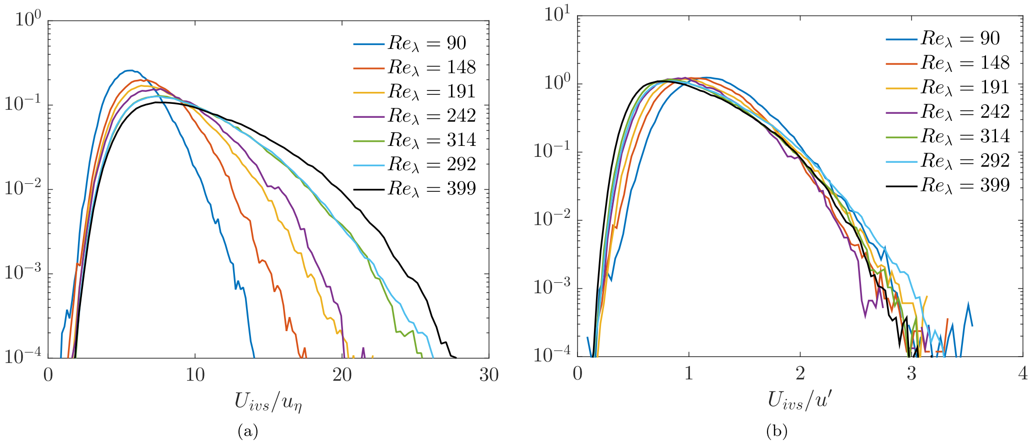

FIG. 8. PDFs of the local tangential velocity of the intense vorticity structures normalized by the (a) local Kolmogorov velocity U_{ivs}/u_η and (b) by the root-mean-square velocity U_{ivs}/u' for all the simulations carried out in the present work.

$\langle U_{ivs}\rangle \sim u'$ is particularly clear in Fig. 7(a) where it is shown that $\langle U_{ivs}\rangle/u_\eta \sim \mathrm{Re}_\lambda^{1/2}$, consistently with this scaling. The results show also that this result is robust and independent of the Reynolds number, again provided that the Reynolds number is sufficiently high, $\mathrm{Re}_\lambda \gtrsim 200$.

In order to assess this scaling in more detail, Figs. 8(a) and 8(b) show the PDFs of U_{ivs}/u_η and U_{ivs}/u', respectively. Clearly, the tangential velocity of the IVS does not scale with the Kolmogorov velocity u_η as the lack of collapse of the several PDFs of U_{ivs}/u_η clearly implies [see Fig. 8(a)]. A similar result is observed for the PDFs of U_{ivs}/u_λ, where $u_\lambda = (\varepsilon\lambda)^{1/3}$ is a velocity scale defined with the Taylor scale (not shown). Visual inspection of Figs. 8(a) and 8(b) suggests that it is reasonable to think that u' is a strong candidate for the scalability of the high-magnitude tail of U_{ivs} (i.e., $U_{ivs}/u' \gtrsim 2$), and it is clear that this U_{ivs} tail does not scale with u_η. Note that the scatter in the high-magnitude tails does not reveal a clear Reynolds number trend and may, therefore, be ascribed to limited convergence. On the other hand, the low-magnitude tail of the U_{ivs} PDF seems to collapse with u_η better than with u' (at least for $\mathrm{Re}_\lambda \gtrsim 200$). This suggests that the U_{ivs} distribution is influenced by both velocity scales, where u' is associated with the most intense vortices and u_η with weaker ones (see also [14]). However, as mentioned above, the mean $\langle U_{ivs}\rangle$ scales with u' and seems unaffected by u_η beyond $\mathrm{Re}_\lambda \gtrsim 200$ (see Fig. 7).

In order to clarify this point we turn to Fig. 9(a), which shows the JPDFs of the local radius R_{ivs} and the local tangential velocity U_{ivs}. It is interesting to see here, more clearly than in [14] due to the higher level of convergence of these plots, the effects of extreme events in the relation between the vortex radius and tangential velocity. Specifically, it is clear that the smaller existing IVS (i.e., smaller radius R_{ivs}) are associated with rare and extreme local tangential velocity events [see Fig. 9(a) near $2 \lesssim R_{ivs}/\eta \lesssim 3$ and $1.5 \lesssim U_{ivs}/u' \lesssim 2.5$]. Conversely, larger local vortex radius are typically associated with smaller tangential velocities [see Fig. 9(a) near $6 \lesssim R_{ivs}/\eta \lesssim 8$ and $U_{ivs}/u' \approx 1.0$]. Moreover, the higher the Reynolds number the stronger this tendency, i.e., the higher the Reynolds number the smaller the IVS and the higher their tangential velocity. The isolines of the JPDFs in Fig. 9(a) are tending into a single line for this range of values, i.e., very small radius and very high tangential velocities, which suggests that the extremely strong IVS scale with u'. However, this u' scaling is not observed for the region representing large vortex radius and small tangential velocities. This fact, i.e., the lack of convergence of the isolines of the joint PDFs for the weak IVS [large radius and small tangential velocities; see the region around near $6 \lesssim R_{ivs}/\eta \lesssim 8$ and $U_{ivs}/u' \approx 1.0$ in Fig. 9(a)], further attests that different scaling laws govern the extreme (very

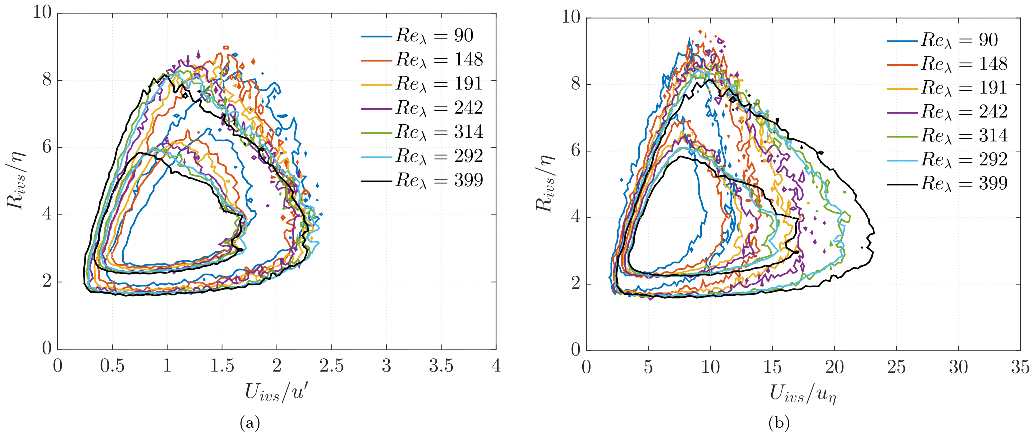

(a)

(b)

FIG. 9. JPDFs of the IVS local radius normalized by the Kolmogorov microscale R_{ivs}/η and the local tangential velocity U_{ivs} for all the simulations carried out in this work: (a) with the local tangential velocity normalized by the root-mean-square velocity, U_{ivs}/u' and (b) with the local tangential velocity normalized by the Kolmogorov velocity U_{ivs}/u_η. Each simulation (or Reynolds number case) is assessed with two contour values. These are equal to 0.1 and 0.01 for figure (a), and 0.01 and 0.001 for figure (b).

weak/very strong) vortex radius/tangential velocity events. Finally, we note that in agreement with [14] the tangential velocity is bounded by $u_\theta \approx 2.5u'$, independently of the Reynolds number.

Figure 9(b) shows the same JPDF of Fig. 9(a) but with the tangential velocity normalized by the Kolmogorov velocity instead. It is clear that a better collapse of the several lines near $6 \lesssim R_{ivs}/\eta \lesssim 8$ and $U_{ivs}/u_\eta \approx 10$ is visible in this figure than in the previous one, which confirms that the local tangential velocity of the larger, less intense, IVS scales better with the Kolmogorov velocity than the root-mean square velocity.

To summarize, the present results confirm that, on average, the tangential velocity of the IVS scales with the root-mean-square velocity $\langle U_{ivs}\rangle \sim u'$ for the range of Reynolds numbers investigated. However, the effects of the extreme events on this scaling become also apparent as the Reynolds number increases, which is due to the fact that higher Reynolds numbers lead to more frequent extreme events and the different role of the small and large velocity scales in the dynamics of the IVS. Whereas U_{ivs} of the extremely strong IVS associated with small R_{ivs} scale with u', the weak IVS scale better with u_η.

C. The length of the intense vorticity structures

In this section we analyze the length scale of the IVS, L_{ivs}, for all the range of Reynolds numbers available in the present work. Note that this characteristic is the one where less results are available in the literature (see Table I) and where less agreement between different authors seems to exist; e.g., some authors claim that the size of the IVS scales with the integral scale of turbulence $\langle L_{ivs}\rangle \sim L$ [13,14], while others suggest it scales with the Taylor microscale, $\langle L_{ivs}\rangle \sim \lambda$ [21]. As we will see these two scaling laws are not observed for Reynolds numbers higher than $\mathrm{Re}_\lambda \gtrsim 200$ and are simply inconsistent with numerous visualizations of IVS recorded in the last two decades.

Figures 10(a) and 10(b) show the mean values of L_{ivs} normalized by the integral scale L and the Kolmogorov microscale η, respectively. Both figures suggest that, instead of $\langle L_{ivs}\rangle \sim L$ or $\langle L_{ivs}\rangle \sim \lambda$, the length of the IVS scales with the Kolmogorov microscale, provided the Reynolds number is sufficiently high. Indeed Fig. 10(a) shows that $\langle L_{ivs}\rangle = 60\eta$ (for $\mathrm{Re}_\lambda \gtrsim 200$), and this scaling law is also supported by Fig. 10(b) where it is clear that $\langle L_{ivs}\rangle/L \sim \mathrm{Re}_\lambda^{-3/2}$, again provided that $\mathrm{Re}_\lambda \gtrsim 200$. However, the results from Fig. 10(b) suggest also that for smaller values of the Reynolds number ($\mathrm{Re}_\lambda \lesssim 180$) the mean length of the IVS scales with the Taylor microscale $\langle L_{ivs}\rangle \sim \lambda$.

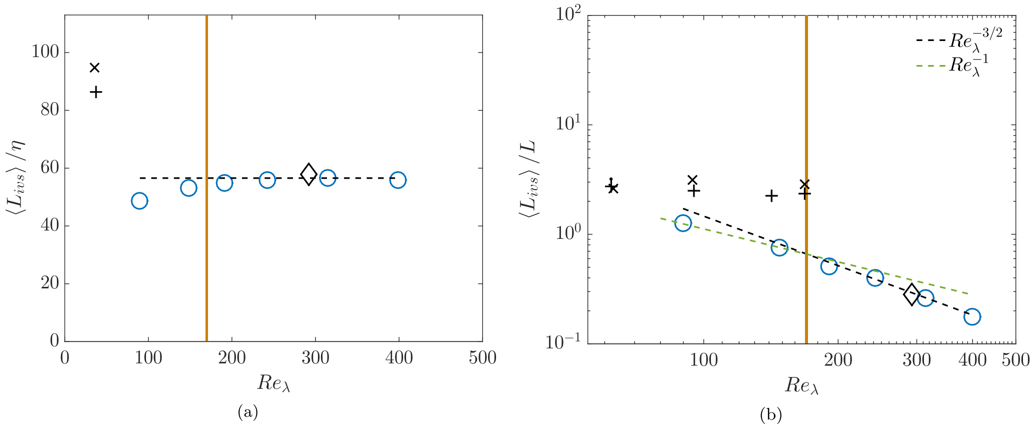

FIG. 10. Mean length of the intense vorticity structures normalized by the (a) Kolmogorov microscale η and (b) integral scale L, as function of the Reynolds number Re_λ, for all the simulations carried out in the present work (blue circles), compared with results obtained in the literature: Jiménez *et al.* [13] ($\times$), Jiménez and Wray [14] ($+$), and Jiménez and Wray [14] ($\cdot$) (DHIT), The black diamond represents the simulation with a smaller integral scale ($\mathrm{Re}_\lambda = 292$), and the vertical orange lines represent the highest Reynolds number previously available in the literature [14]. The black dashed line corresponds to (a) a constant value and (b) a power law with $\sim\mathrm{Re}_\lambda^{-3/2}$, while the green dashed line in (b) corresponds to $\sim\mathrm{Re}_\lambda^{-1}$.

In order to investigate this result further, Figs. 11(a) and 11(b) show that PDFs of the length of the IVS normalized by the integral scale of turbulence L_{ivs}/L and the Kolmogorov microscale L_{ivs}/η, respectively. The PDFs are approximately exponential, which agrees with the observations described in [14]; however, the present figures strongly support a Kolmogorov scaling for the length of the IVS. Indeed, Fig. 11(a) shows that the peak of the PDFs of L_{ivs}/L shifts to the left for increasing values of the Reynolds number, which is inconsistent with the scaling $L_{ivs} \sim L$ assumed in many previous works. In contrast Fig. 11(b) shows that the PDFs of L_{ivs}/η nicely collapse into the same curve for all but the smallest Reynolds numbers considered in the present work ($\mathrm{Re}_\lambda = 90$ and 148). Thus, it is clear that the length of the IVS scales with the Kolmogorov microscale, and not with either the integral scale of turbulence or the Taylor microscale (at high Reynolds numbers).

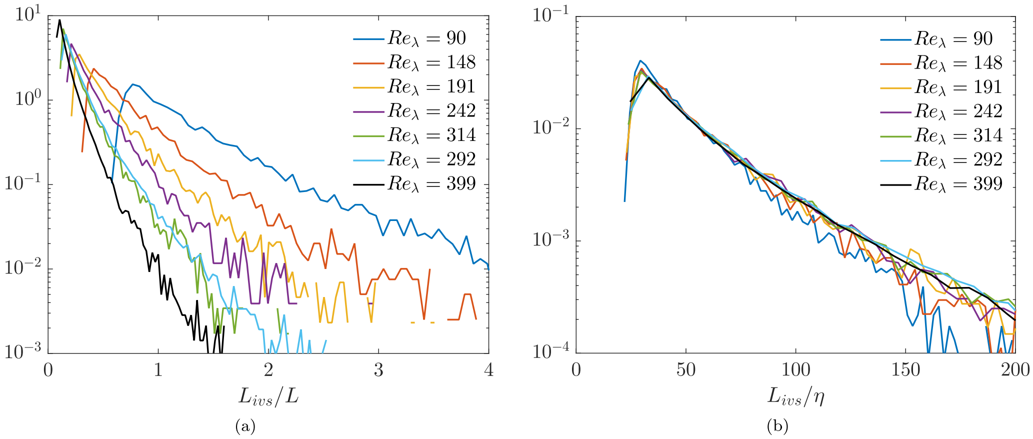

FIG. 11. PDFs of the local length of the intense vorticity structures normalized by the (a) integral scale L and (b) by the Kolmogorov microscale η for all the simulations carried out in the present work.

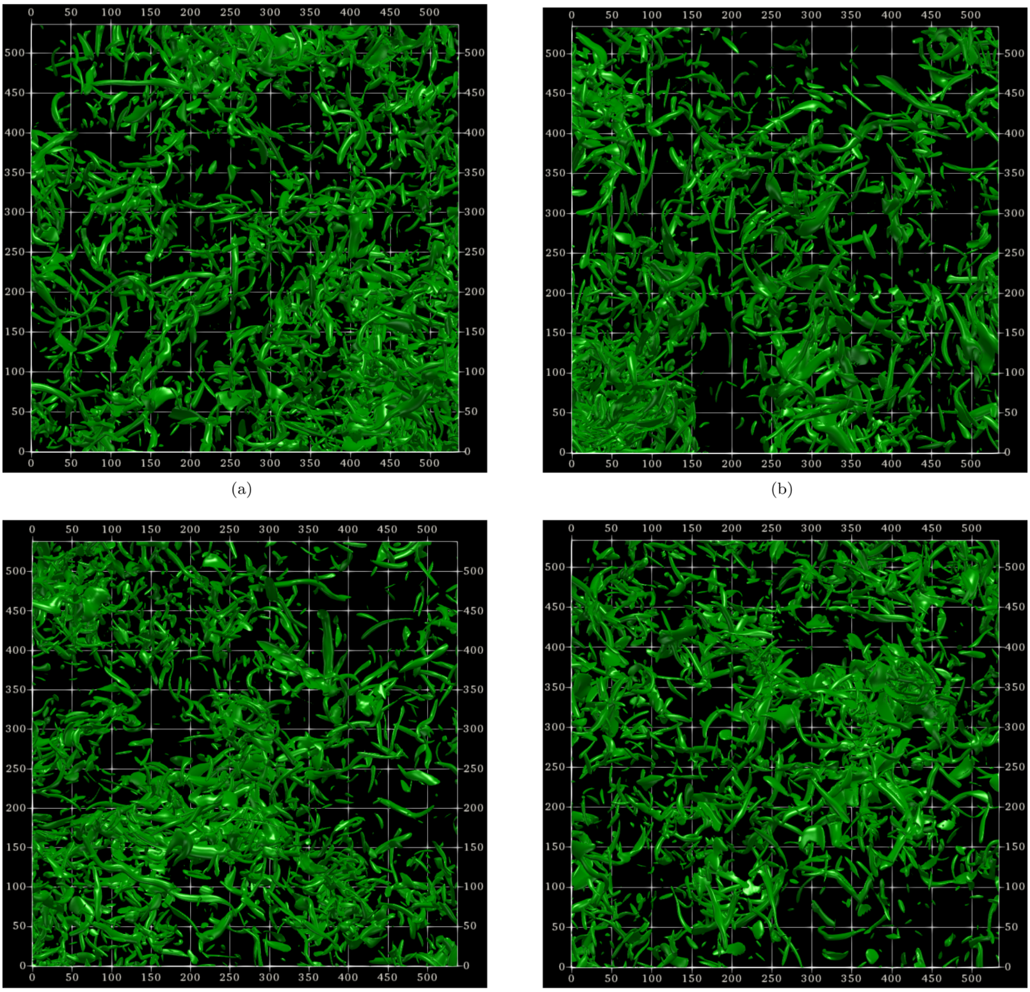

(a)

(b)

(c)

(d)

FIG. 12. Isosurfaces of vorticity magnitude corresponding to the volume occupied by the 1% most intense vorticity showing only a fraction of the computational domain for the DNS with (a) $N^3 = 768^3$ ($\mathrm{Re}_\lambda = 191$); (b) $N^3 = 1024^3$ ($\mathrm{Re}_\lambda = 242$); (c) $N^3 = 1536^3$ ($\mathrm{Re}_\lambda = 314$); and (d) $N^3 = 2048^3$ ($\mathrm{Re}_\lambda = 399$). The panels show only the subregions indicated by white squares in Fig. 1, where the labels indicate the coordinates in units of $\Delta x/\eta$, $\Delta y/\eta$ and $\Delta z/\eta$; i.e., for each simulation the maximum extent of the subdomain shown is approximately $(512\eta \times 512\eta \times 512\eta)$.

The mean length normalized by the Taylor microscale follows the scaling relation $L_{ivs}/\lambda \sim \mathrm{Re}_\lambda^{-1/2}$, which also supports a Kolmogorov scaling (not shown), while the PDFs of L_{ivs}/λ are qualitatively similar to the ones of L_{ivs}/L and do not support integral or Taylor scaling of L_{ivs} (not shown).

The correct scaling of $L_{ivs} \sim \eta$ may have been "right before our eyes" for several years as the isosurfaces in Figs. 12(a) to 12(d) attest. These figures show the small (bottom-left) subdomains displayed before in Fig. 1 (with the same isosurfaces of vorticity magnitude) and concern only the higher Reynolds numbers analyzed here with $\mathrm{Re}_\lambda = 191$–$399$. Notice that the subdomains have been chosen so that the same size (in Kolmogorov units) is shown in the four cases, with dimensions of approximately $(512\eta \times 512\eta \times 512\eta)$. It is clearly not possible to identify which figures correspond to which (higher or lower) Reynolds number cases by simple visual inspection.

Indeed, all the figures seem to represent the same flow. This simply reflects the fact that the same aspect ratio L_{ivs}/R_{ivs} is observed for all IVS, independently of the Reynolds number, which is possible to observe only if these two IVS characteristics equally scale with the Kolmogorov microscale as has been shown here, so that $\langle L_{ivs}\rangle/\langle R_{ivs}\rangle \approx 60\eta/4\eta \approx 15$. A visual measurement of the identified IVS in Figs. 12(a) to 12(d) was carried out and confirms this constant value of approximately 15.

The present scaling results for the length of the IVS, $L_{ivs} \sim \eta$, are consistent with the average flow structure in the strain eigenframe, which reveals 90η long vortices over a wide range of Reynolds numbers [23] and consists of yet other evidence that this average in the strain eigenframe is representative of the instantaneous flow structures. The reported length in [23], i.e., 90η, is longer than the present average length of 60η, which can be explained by the lower vorticity threshold used to determine this length in that previous work; however, the scaling with η is consistent in the present work and [23] since the magnitude of the prefactor (90 vs 60) is of the same order of magnitude. It is noteworthy that Elsinga *et al.* [23] also showed that the vortex stretching motions are fully developed and Reynolds number independent when Re_λ exceeds approximately 250. At lower Reynolds numbers, the stretching motions, which scale with λ, are smaller than the characteristic length of the small-scale structures, which scale with η. This restricts the length of the IVS for $\mathrm{Re}_\lambda \lesssim 250$. Indeed, the mean length of the IVS $\langle L_{ivs}\rangle$ follows a Taylor scaling at low Reynolds (limited by the stretching motions) and Kolmogorov scaling at high Reynolds, when the size of the stretching motions is no longer limiting. Jiménez and Wray [14] also found a Taylor scaling at low Reynolds numbers when L_{ivs} is based on the vorticity autocorrelation length along the vortex axis. However, the $\mathrm{Re}_\lambda > 250$ regime could not be reached in their simulations, which go only until $\mathrm{Re}_\lambda = 168$, and therefore the ultimate Kolmogorov scaling has remained unnoticed until now. Recent scaling laws needing a threshold Reynolds number of about $\mathrm{Re}_\lambda > 200$–$250$ to be observed include the determination of the correct scaling of the turbulent/nonturbulent interface layer [24] and the velocity-gradient structure in turbulent flows [25].

Note that Jiménez and Wray [14] used a second definition for L_{ivs}, which resulted in L scaling (actually their figure for $\langle L_{ivs}\rangle/L$ shows a slight decrease as the Reynolds number increases). In their case the worm tracking was terminated when the vorticity dropped below ω'. This vorticity threshold is much lower than the presently used value and represents the background vorticity level. Therefore, it is expected to yield longer vortices but not necessarily a $L_{ivs} \sim L$ scaling. However, a $L_{ivs} \sim L$ scaling would be consistent with IVS clustering within shear layers, which bound large-scale quasiuniform flow regions as observed in [31,32]. These large-scale shear layers contain approximately uniform background vorticity (of order ω'), and therefore, continuous vortex lines may be traced within them over distances of order L. Higher thresholds, such as used here and implied when using the vorticity autocorrelation, cause the IVS to separate from the background leading to a different scaling of their length.

We finish this section by recalling the observations made in the first chapter of [22] that the dependence of the length scale of the "worms" "on Re_λ is similar to that of η, rather than that of λ; nevertheless their values are closer to λ than to η." This shows that their observations agree with the present results, but the suggestion that $L_{ivs} \sim \lambda$ in our opinion misses out the important fact that the value of a variable has no direct link with the true scaling law. Indeed, the values of L_{ivs} are of the order of L or λ (depending on the Reynolds number), but this has no information on the true scaling law. Another example already mentioned above consists on the mean thickness of the turbulent/nonturbulent interface layer δ_ω, which is typically one order of magnitude bigger than the Kolmogorov microscale $\langle\delta_\omega\rangle/\eta \approx 10$–$16$ and yet it clearly scales with the Kolmogorov microscale for sufficiently high Reynolds numbers [24].

Finally, the interesting problem of determining how the IVS are formed deserves a few comments. It is plausible that the IVS originate from vortex sheet structures existing within the flow field which roll up into "worms" due to the Kelvin-Helmholtz instability [1], but apart from a few studies, e.g., [33], not much has been done to investigate this process, and even less to see how it might be affected at high Reynolds numbers. We have carried out a few animations of the evolution of the IVS, which seem to confirm that, as suggested in [13], these structures are not formed in a single stage, but instead seem to grow or coalesce during their lifetimes. However, a proper analysis of the emergence, evolution, and decay of the "worms" in our opinion can be achieved only by a detailed analysis of the detected IVS as a function of time and cannot be investigated using only one instantaneous velocity field. This issue should be addressed in future works.

V. CONCLUSIONS

One of the most notable features of turbulent flows is the presence of a range of eddy structures, typically defined as regions of concentrated vorticity and low pressure, that have a life time which is comparable to the characteristic time of the large scales of the flow [2]. Among these are the so-called intense vorticity structures (IVS), which constitute regions of particularly intense vorticity, having, however, a negligible kinetic energy content and giving a negligible contribution to the total viscous dissipation.

Jiménez *et al.* [13,14] defined these structures as flow structures with the highest local values of enstrophy contained in 1% of the volume of the flow. Although the majority of the works devoted to these structures focused in homogeneous isotropic turbulence (HIT) similar IVS are found in several inhomogeneous flows such as in turbulent channel flows and turbulent mixing layers [12].

In the present work we analyze the characteristics of these structures as function of the Reynolds number, by exploring much higher Reynolds numbers than previously available, i.e., available in the classical works devoted to the investigation of these structures. Specifically, we use direct numerical simulations (DNS) of HIT, carried out with classical pseudospectral methods and with Taylor-based Reynolds numbers in the range $90 \leqslant \mathrm{Re}_\lambda \leqslant 399$, for a resolution of $k_{\max}\eta = 2$, where $k_{\max}$ is the maximum resolved wave number and η is the Kolmogorov's microscale.

The results show that many of the results obtained in the classical works are relatively independent of the Reynolds number, e.g., the mean radius of the IVS is approximately $\langle R_{ivs}\rangle/\eta \approx 4$–5, and the mean radius is equal to radius of the stationary Burgers vortex $\langle R_{ivs}/R_B\rangle \approx 1.0$ [14]. However, the same is not true for the length of the IVS (L_{ivs}), which is here defined by computing the length of a path aligned with the local vorticity vector, where the enstrophy is above the threshold defining the IVS. Previous works have claimed that the mean length of the IVS scales with the integral scale of the flow $\langle L_{ivs}\rangle \sim L$, while other works suggest it scales with the Taylor microscale $\langle L_{ivs}\rangle \sim \lambda$. It turns out that although $\langle L_{ivs}\rangle$ is often of the order of L it scales with the Kolmogorov microscale for Reynolds numbers above $\mathrm{Re}_\lambda \gtrsim 200$. Indeed, the results clearly show that for sufficiently high Reynolds numbers $\langle L_{ivs}\rangle \approx 60\eta$ and that $\langle L_{ivs}\rangle/L \sim \mathrm{Re}_\lambda^{-3/2}$, which is consistent with a Kolmogorov scaling of L_{ivs}. Nevertheless, for small Reynolds numbers ($\mathrm{Re}_\lambda \lesssim 200$) the results also indicate a scaling with the Taylor scale $\langle L_{ivs}\rangle \sim \lambda$ as claimed by some authors.

An even more compelling demonstration of the Kolmogorov scaling of L_{ivs} at high Reynolds numbers is given by the PDFs of the L_{ivs}. The PDFs of L_{ivs} computed at different Reynolds numbers collapse nicely into the same curve when normalized by the Kolmogorov microscale, provided the Reynolds number is sufficiently high ($\mathrm{Re}_\lambda \gtrsim 200$). This collapse is not observed when the PDFs of L_{ivs} are normalized by the integral scale of turbulence or by the Taylor microscale.

Katsunori *et al.* [34] have shown that the statistics of the large scales in HIT are not sensitive to the small-scale dynamics and vortex structures, but this last result may have implications for the study of small-scale intermittency in turbulence, since intermittency results from the most extreme events existing within the flow from which the IVS are an example.

ACKNOWLEDGMENTS

C.B.S. acknowledges Javier Jiménez for interesting discussions on this topic that led to Appendixes C and D. C.B.S. acknowledges Fundação para a Ciência e Tecnologia (FCT) through IDMEC, underLAETA, Project No. UIDB/50022/2020. A.A.G. acknowledges Fundação para a Ciência e Tecnologia (FCT) through Contract No. 2021.08206.BD. C.B.S. acknowledges HPC computing and consulting resources that have contributed to the research results reported within this paper [35]. The authors acknowledge the Laboratory for Advanced Computing at University of Coimbra for providing HPC, computing, and consulting resources [36]. C.B.S acknowledges Fundação para a Ciência e Tecnologia (FCT) through projects PCIF/GFC/0109/2017 and PCIF/MPG/0147/2019.

APPENDIX A: NUMERICAL METHODS

The simulations used in the present work are carried out with a highly accurate in-house Navier-Stokes solver using classical pseudospectral methods for spatial discretization, while a three-stage, third-order Runge-Kutta scheme is used for temporal advancement. The simulations are carried out in a three-dimensional periodic box of sizes $2\pi \times 2\pi \times 2\pi$ using N^3 collocation points and are fully dealiased with the $2/3$ rule. The code is parallelized with MPI using the 2DECOMP library [37] and has been used in several previous works. More details are given in [24] and references therein.

Following the classical procedure using pseudospectral methods the Navier-Stokes equations are transformed into the Fourier space through the application of the three-dimensional (direct) Fourier transform ($F\{\}$),

$$\widehat{u_i}(\vec{k},t) = F\{u_i(\vec{x},t)\} = \frac{1}{N^3}\sum_{\vec{x}} u_i(\vec{x},t)\exp(-i\vec{k}\cdot\vec{x}), \tag{A1}$$

while the inverse transform ($F^{-1}\{\}$), defined by

$$u_i(\vec{x},t) = F^{-1}\{\widehat{u_i}(\vec{k},t)\} = \sum_{\vec{k}} \widehat{u_i}(\vec{k},t)\exp(+i\vec{k}\cdot\vec{x}) \tag{A2}$$

is used to recover the fields in physical space (i is the imaginary unit). In these equations $u_i(\vec{x},t)$ ($i = 1, 2, 3$) is the physical space velocity field at time t and at the discrete coordinates $\vec{x}$ in the physical space, while $\widehat{u_i}(\vec{k},t)$ are the Fourier coefficients at the discrete wave vectors $\vec{k}$, with components $k = -N/2, \ldots, -1, 0, +1, \ldots, N/2 - 1$. The grid spacing in the physical space is then $\Delta x = L_{box}/N = 2\pi/N$, whereas in the Fourier space we have $\Delta k = 2\pi/L_{box} = 1$.

The temporal evolution of the Fourier coefficients of the velocity field is given by the transformed momentum equations,

$$\frac{\partial\widehat{u_i}(\vec{k},t)}{\partial t} + \nu k^2\widehat{u_i}(\vec{k},t) = -\left(\delta_{ij} - \frac{k_i k_j}{k^2}\right)\widehat{N_j}(\vec{k},t) + \widehat{f}(\vec{k},t), \tag{A3}$$

where $\widehat{N_i}(\vec{k},t) = \mathrm{i}k_j\widehat{u_i u_j}(\vec{k},t)$ is the nonlinear term from the Navier-Stokes equations, $k^2 = k_i k_i$ is the square of the magnitude of wave number vector $\vec{k}$, and $\widehat{f}(\vec{k},t)$ is the artificial forcing needed to sustain the turbulence.

The present Navier-Stokes solver uses the forcing scheme described by Alvelius [26], where the forcing function $f(\vec{x},t)$ is delta correlated in time and uncorrelated with the velocity field, and ensures that on average the power input of the forcing balances the viscous dissipation rate, $P = \varepsilon$, where $P = \langle f_i u_i\rangle$ (the brackets represent a volume average). The forcing function has a Gaussian shape which concentrates the power input into a small range of wave numbers, centred at a given peak wave number k_p. All simulations use an input power equal to $P = 10$, which is concentrated in the first two wave numbers centered at $k_p = 2$, except for the simulation with $\mathrm{Re}_\lambda = 292$, where the forcing is imposed in the first four wave numbers centered at $k_p = 4$.

The integral flow quantities are computed directly from the kinetic energy spectrum, which is defined by

$$E(k) = 4\pi k^2 \left\langle \tfrac{1}{2}\widehat{u}_i(\vec{k},t)\widehat{u}_i^*(\vec{k},t)\right\rangle_{|\vec{k}|}, \tag{A4}$$

where "*" represents the complex conjugate and $\langle\widehat{\phi}\rangle_{|\vec{k}|}$ denotes the spherical-shell average of the quantity $\widehat{\phi}$, i.e.,

$$\langle\widehat{\phi}(\vec{k},t)\rangle_{|\vec{k}|} = \frac{1}{N_k}\sum_{k-\frac{\Delta k}{2}<k<k+\frac{\Delta k}{2}} \widehat{\phi}(\vec{k},t). \tag{A5}$$

This summation is carried out over all the N_k modes within a shell (of thickness $\Delta k = 1$) centered at $k = |\vec{k}|$. The turbulent kinetic energy K, and the viscous dissipation rate ε, are computed with

$$K = \sum_{k_{min}}^{k_{\max}} E(k)\Delta k \tag{A6}$$

and

$$\varepsilon = 2\nu\sum_{k_{min}}^{k_{\max}} k^2 E(k)\Delta k, \tag{A7}$$

respectively, with $k_{\max} = N/3$ due to the dealisiang method use here. Finally, the integral, Taylor and Kolmogorov microscales are given by

$$L = \left(\frac{\pi}{2K}\right)\sum_{k_{min}}^{k_{\max}} \frac{E(k)}{k}\Delta k, \tag{A8}$$

$$\lambda = \sqrt{\frac{10\nu K}{\varepsilon}}, \tag{A9}$$

and

$$\eta = \left(\frac{\nu^3}{\varepsilon}\right)^{1/4}, \tag{A10}$$

respectively, and the Reynolds number based on the Taylor microscale is defined by

$$\mathrm{Re}_\lambda = \sqrt{\frac{2K}{3}}\frac{\lambda}{\nu}. \tag{A11}$$

APPENDIX B: WORMTRACKER ALGORITHM

For computing the characteristics of the IVS the WORMTRACKER algorithm starts by defining the vorticity threshold magnitude corresponding to the IVS. As in [13,14] the IVS are defined as flow points with the highest vorticity magnitude covering 1% of the total flow domain. Once these points have been identified the axis of each IVS is defined by choosing the points with the highest value of the local vorticity magnitude, and where the direction of the local vorticity is used to assess the location of the next neighboring axis point. Once each of the individual axis points for each IVS has been determined, the vorticity is sampled in a local plane which is perpendicular to the local vorticity vector at that point [see Fig. 2(b)]. After this assignment, axis that have less than 20 points are discarded, and clustered axis points are eliminated, leaving only axis points with highest vorticity magnitude. More details on this process are given in [5].

In order to compute the IVS statistics, such as worm radius and circulation, at each point of each IVS axis, the vorticity profile is interpolated (using the least squares method) into the plane

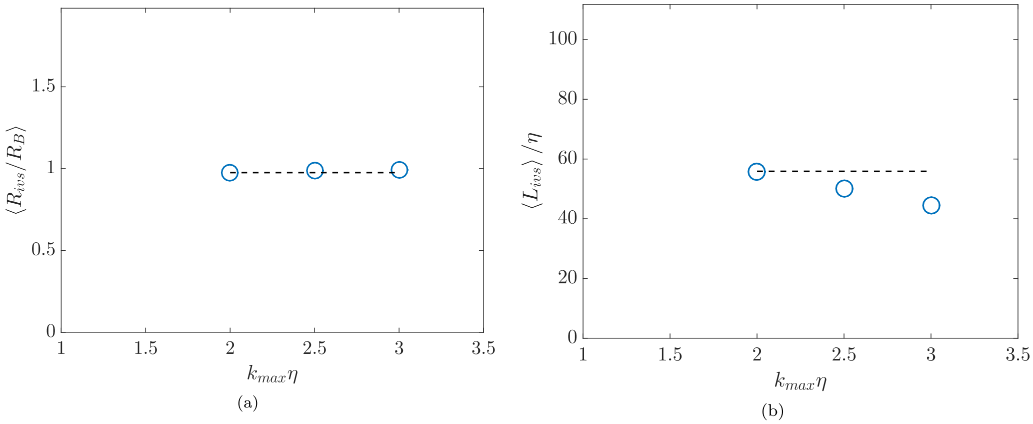

FIG. 13. (a) Mean radius of the intense vorticity structures normalized by the local Burgers radius $\langle R_{ivs}/R_B \rangle$ and (b) mean length of the intense vorticity structures normalized by the Kolmogorov microscale $\langle L_{ivs} \rangle / \eta$ for three simulations with $N^3 = 1024^3$: one with $k_{\max}\eta = 2.0$ and $\mathrm{Re}_\lambda = 242$ (listed in Table II) and two others with $k_{\max}\eta = 2.5$ and $k_{\max}\eta = 3.0$ and Reynolds numbers of $\mathrm{Re}_\lambda = 210$ and $\mathrm{Re}_\lambda = 180$, respectively.

perpendicular to local vorticity vector. The set of discrete points used in this plane (normal to the local vorticity vector) is defined in a cylindrical coordinate system $(r;\theta)$, where $r = 0$ at the axis, whose coordinates are given by $(n_r \Delta x; 2\pi m_\theta / M_\theta)$, with $n_r = 0, \ldots, N_r$ and $m_\theta = 0, \ldots, M_\theta$, where N_r and M_θ are the radial and azimuthal number of points, respectively. To compensate for any noise induced by the interpolation the radial distribution is filtered over triples of consecutive axial location using a $[1/4; 1/2; 1/4]$ mask.

As described in Sec. III the local radius of each IVS axis R_{ivs} is computed by an iterative process using the radial vorticity distribution and assuming it to have a Gaussian shape, defined in Eq. (7). In this process local radius values where the algorithm did not converge were discarded, as well as those where the local radius was $R_{ivs} > 30\eta$. The local azimutal velocity U_{ivs} is computed directly from the local velocity field, projected into a plane perpendicular to the local vorticity. Finally, the worm length L_{ivs} of each IVS is computed as the sum of all $\mathrm{d}L_{ivs}$ detected during the construction of the axis of the structure.

APPENDIX C: INFLUENCE OF RESOLUTION EFFECTS ON THE STATISTICS OF THE INTENSE VORTICITY STRUCTURES

The initial work described in the main text of this paper was done using another set of simulations where a smaller resolution of $k_{\max}\eta = 1.5$ was employed (not shown). Later we carried out a new set of simulations (discussed in the core of the present work and listed in Table II) where the resolution was increased to $k_{\max}\eta = 2.0$. It was observed that all the scaling laws described in this work are equal using either $k_{\max}\eta = 1.5$ or $k_{\max}\eta = 2.0$, but we finally decided to use only the simulations with the higher resolution $k_{\max}\eta = 2.0$, as this is the same resolution used in [13,14] where this issue was first discussed.

The influence of the resolution on the statistics of the IVS was further investigated by carrying out two additional (new) simulations with different resolutions. As reference we use the simulation with $N^3 = 1024^3$ collocation points and $\mathrm{Re}_\lambda = 242$ (listed in Table II), and we carried out two new simulations with $N^3 = 1024^3$ where we kept all the computational parameters fixed and equal to the reference simulation and changed only the kinematic viscosity. By varying the kinematic viscosity between $\nu = 0.003$ and $\nu = 0.004$ we obtained Reynolds numbers of $\mathrm{Re}_\lambda = 210$ and $\mathrm{Re}_\lambda = 180$, and resolutions of $k_{\max}\eta = 2.5$ and $k_{\max}\eta = 3.0$, respectively.

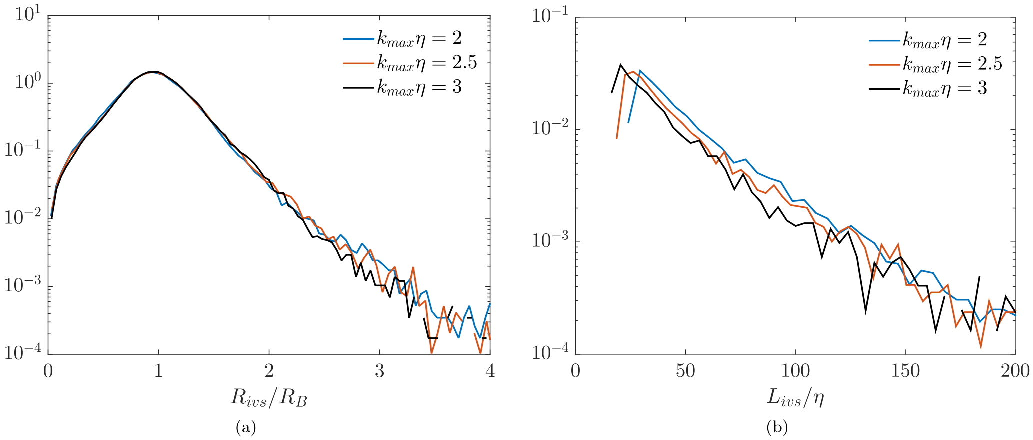

FIG. 14. PDFs of the (a) local radius of the intense vorticity structures normalized by local Burgers radius R_{ivs}/R_B and (b) local length of the intense vorticity structures normalized by the Kolmogorov microscale L_{ivs}/η for three simulations with $N^3 = 1024^3$: one with $k_{\max}\eta = 2.0$ and $\mathrm{Re}_\lambda = 242$ (listed in Table II) and two others with $k_{\max}\eta = 2.5$ and $k_{\max}\eta = 3.0$ and Reynolds numbers of $\mathrm{Re}_\lambda = 210$ and $\mathrm{Re}_\lambda = 180$, respectively.

Figures 13(a) and 13(b) show the mean radius of the intense vorticity structures normalized by the local Burgers radius $\langle R_{ivs}/R_B\rangle$ and the mean length of the intense vorticity structures normalized by the Kolmogorov microscale $\langle L_{ivs}\rangle/\eta$, respectively, for the three simulations. There is virtually no effect on the mean radius of the IVS and only a mild influence on the mean length of the IVS that, however, does not affect the scaling laws described in this paper, as confirmed by the initial set of simulations carried out in this work using $k_{\max}\eta = 1.5$: only the scaling constant for the length is slightly affected but remains on the same order of magnitude.

Figures 14(a) and 14(b) show the PDFs of the local radius of the intense vorticity structures normalized by local Burgers radius R_{ivs}/R_B and the local length of the intense vorticity structures normalized by the Kolmogorov microscale L_{ivs}/η, respectively, for the three simulations. Again the resolution has virtually no effect on the vortex radius normalized by the local Burgers radius and only a very small effect on the PDF of $\langle L_{ivs}\rangle/\eta$, which in any case does not affect the conclusions from the present work.

APPENDIX D: INFLUENCE OF THE THRESHOLD ON THE STATISTICS OF THE INTENSE VORTICITY STRUCTURES

The influence of the value of the vorticity threshold ω_{ivs} in the results of the IVS characteristics was investigated using the simulation with $N^3 = 1024^3$ and $\mathrm{Re}_\lambda = 242$ listed in Table II. As described in Sec. III the IVS analyzed here are defined as flow points with the highest vorticity magnitude covering 1% of the total flow domain, in agreement with most of the existing works assessing these structures, starting with [13]. In this Appendix we describe the IVS characteristics obtained with four different values of the vorticity magnitude threshold ω_{ivs} used to defined the IVS, where ω_{ivs} corresponds to the flow points with the highest vorticity magnitude covering 1%, 2%, 3%, and 4% of the total flow domain.

Figures 15(a) and 15(b) show the mean values of the vortex radius normalized by the Burgers radius $\langle R_{ivs}/R_B\rangle$ and of the mean length normalized by the Kolmogorov microscale $\langle L_{ivs}\rangle/\eta$, respectively, for the simulation with $N^3 = 1024^3$ and $\mathrm{Re}_\lambda = 242$. As can be observed the value of the threshold does not affect the value of the IVS radius since we have $\langle R_{ivs}/R_B\rangle \approx 1.0$, for 1% to 4%. The same can be said regarding the length scale of the IVS, which is always $\langle L_{ivs}\rangle/\eta \approx 60$,

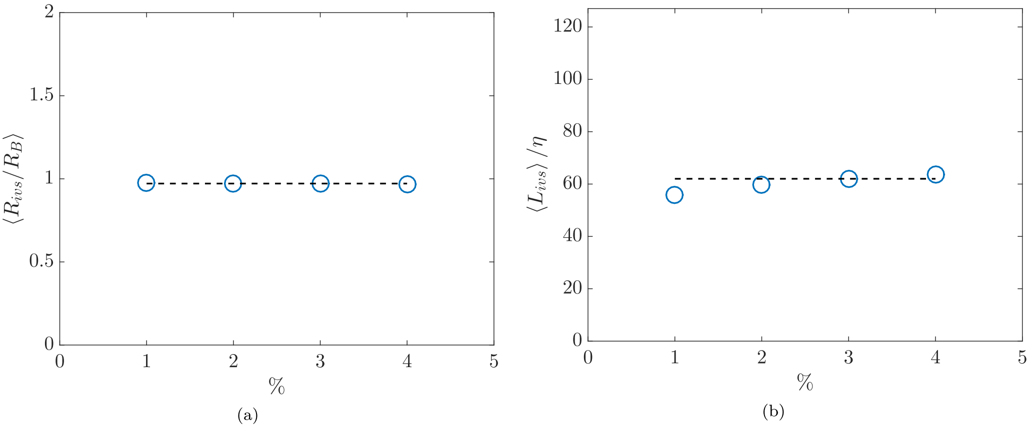

FIG. 15. (a) Mean radius of the intense vorticity structures normalized by the local Burgers radius $\langle R_{ivs}/R_B \rangle$ and (b) mean length of the intense vorticity structures normalized by the Kolmogorov microscale $\langle L_{ivs} \rangle/\eta$, for the simulation with $N^3 = 1024^3$ and $\text{Re}_\lambda = 242$. The statistics correspond to the points with the highest vorticity covering 1%, 2%, 3%, and 4% of the total flow domain.

with minor deviations from this value, on the order of the variations observed when changing the Reynolds number of the flow as documented in Fig. 4(b).

Figures 16(a) and 16(b) show the PDFs for the local radius of the intense vorticity structures normalized by local Burgers radius R_{ivs}/R_B and of the local length of the intense vorticity structures normalized by the Kolmogorov microscale L_{ivs}/η, respectively, for the simulation with $N^3 = 1024^3$ and $\text{Re}_\lambda = 242$. It is clear that these PDFs are almost equal, with the only difference arising from the slight improved convergence of the curves corresponding to 4% due to the higher number of

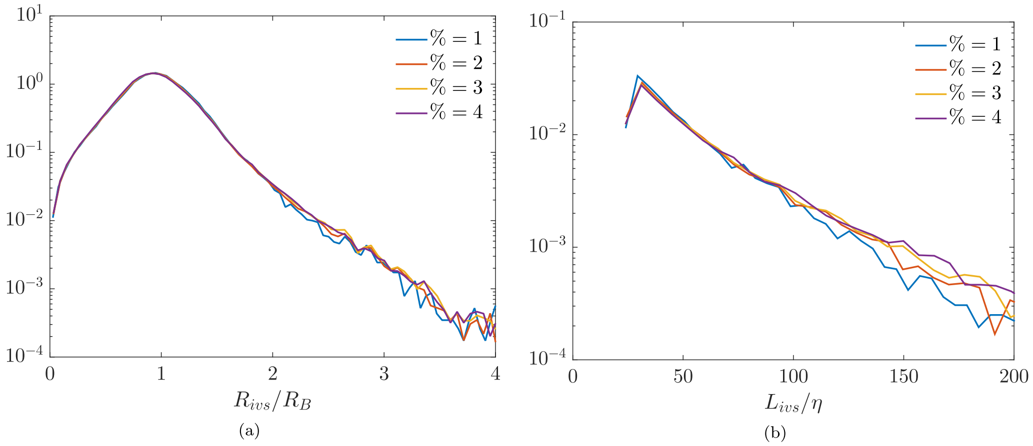

FIG. 16. PDFs of the (a) local radius of the intense vorticity structures normalized by local Burgers radius R_{ivs}/R_B and (b) local length of the intense vorticity structures normalized by the Kolmogorov microscale L_{ivs}/η for the simulation with $N^3 = 1024^3$ and $\text{Re}_\lambda = 242$. The statistics correspond correspond to the points with the highest vorticity covering 1%, 2%, 3%, and 4% of the total flow domain.

available flow points to compute the statistics. Note that these small differences do not affect in any way the scaling laws but only (very slightly) the scaling constant, which in any case is always $\langle L_{ivs}\rangle/\eta \approx 60$.

Similar results are obtained when analyzing the other IVS characteristics and show that the value of the threshold defining the IVS has a negligible effect on the results described in the present work and no effect in the conclusions, provided this threshold is close to 1%.

[1] P. A. Davidson, *Turbulence: An Introduction for Scientists and Engineers*, 2nd ed. (Oxford University Press, Oxford, 2015).

[2] E. Villermaux, B. Sixou, and Y. Gagne, Intense vortical structures in grid-generated turbulence, Phys. Fluids **7**, 2008 (1995).

[3] T. Ishihara, Y. Kaneda, M. Yokokawa, K. Itakura, and A. Uno, Small-scale statistics in high-resolution direct numerical simulation of turbulence: Reynolds number dependence of one-point velocity gradient statistics, J. Fluid Mech. **592**, 335 (2007).

[4] S. Kida and H. Miura, Identification and analysis of vortical structures, Eur. J. Mech. B: Fluids **17**, 471 (1998).

[5] C. B. da Silva, R. J. N. dos Reis, and J. C. F. Pereira, The intense vorticity structures near the turbulent/non-turbulent interface in a jet, J. Fluid Mech. **685**, 165 (2011).

[6] O. Cadot, S. Douady, and Y. Couder, Characterization of the low-pressure filaments in a three-dimensional turbulent shear flow, Phys. Fluids **7**, 630 (1995).

[7] E. D. Siggia, Numerical study of small-scale intermittency in three-dimensional turbulence, J. Fluid Mech. **107**, 375 (1981).

[8] R. Kerr, Higher order derivative correlation and the alignment of small-scale structures in isotropic turbulence, J. Fluid Mech. **153**, 31 (1985).

[9] Z.-S. She, E. Jackson, and S. Orszag, Structure and dynamics of homogeneous turbulence: Models and simulations, Proc. R. Soc. London A **434**, 101 (1991).

[10] A. Vincent and M. Meneguzzi, The spatial structure and statistical properties of homogeneous turbulence, J. Fluid Mech. **225**, 1 (1991).

[11] S.-J. Kang, M. Tanahashi, and T. Miyauchi, Dynamics of fine scale eddy clusters in turbulent channel flows, J. Turbul. **8**, 52 (2007).

[12] M. Tanahashi, S. Iwase, and T. Miyauchi, Appearance and alignment with strain rate of coherent fine scale eddies in turbulent mixing layer, J. Turbul. **2**, 1 (2001).

[13] J. Jiménez, A. Wray, P. Saffman, and R. Rogallo, The structure of intense vorticity in isotropic turbulence, J. Fluid Mech. **255**, 65 (1993).

[14] J. Jiménez and A. Wray, On the characteristics of vortex filaments in isotropic turbulence, J. Fluid Mech. **373**, 255 (1998).

[15] G. R. Ruetsch and M. R. Maxey, Small-scale features of vorticity and passive scalar fields in homogeneous isotropic turbulence, Phys. Fluids **3**, 1587 (1991).

[16] G. R. Ruetsch and M. R. Maxey, The evolution of small-scale structures in homogeneous isotropic turbulence, Phys. Fluids **4**, 2747 (1992).

[17] A. Vincent and M. Meneguzzi, The dynamics of vorticity tubes in homogeneous turbulence, J. Fluid Mech. **258**, 245 (1994).

[18] B. Ganapathisubramani, K. Lakshminarasimhan, and N. T. Clemens, Investigation of three-dimensional structure of fine scales in a turbulent jet by using cinematographic stereoscopic particle image velocimetry, J. Fluid Mech. **598**, 141 (2008).

[19] H. Mouri, A. Houri, and Y. Kawashima, Laboratory experiments for intense vortical structures in turbulence velocity fields, Phys. Fluids **19**, 055101 (2007).

[20] T. Watanabe, R. Jaulino, R. R. Taveira, C. B. da Silva, K. Nagata, and Y. Sakai, Role of an isolated eddy near the turbulent/non-turbulent interface layer, Phys. Rev. Fluids **2**, 094607 (2017).

[21] K. Yamamoto and I. Hosokawa,A decaying isotropic turbulence pursued by the spectral method, J. Phys. Soc. Jpn. **57**, 1532 (1988).

[22] P. A. Davidson, Y. Kaneda, and K. Sreenivasan, *Ten Chapters of Turbulence* (Cambridge University Press, Cambridge, 2013).

[23] G. Elsinga, T. Ishihara, M. V. Goudar, C. B. da Silva, and J. C. R. Hunt, The scaling of straining motions in homogeneous isotropic turbulence, J. Fluid Mech. **829**, 31 (2017).

[24] T. S. Silva, M. Zecchetto, and C. B. da Silva, The scaling of the turbulent/non-turbulent interface at high Reynolds numbers, J. Fluid Mech. **843**, 156 (2018).

[25] R. Das and S. S. Girimaji, On the Reynolds number dependence of velocity-gradient structure and dynamics, J. Fluid Mech. **138617**, 163 (2019).

[26] K. Alvelius, Random forcing of three-dimensional homogeneous turbulence, Phys. Fluids **11**, 1880 (1999).

[27] T. I. T, K. Morishita, M. Yokokawa, A. Uno, and Y. Kaneda, Polymer-induced drag reduction: Effects of the variations in elasticity and inertia in turbulent viscoelastic channel flow, Phys. Rev. Fluids **1**, 082403(R) (2016).

[28] D. Buaria, A. Pumir, E. Bodenschatz, and P. K. Yeung, Extreme velocity gradients in turbulent flows, New J. Phys. **21**, 043004 (2019).

[29] K. Ravikumar, D. Appelhans, and P. K. Yeung, GPU acceleration of extreme scale pseudo-spectral simulations of turbulence using asynchronism, in *Proceedings of the International Conference for High Performance Computing, Networking, Storage and Analysis, SC'19* (ACM, New York, 2019), pp. 1–22.

[30] G. Elsinga, T. Ishihara, and J. Hunt, Extreme dissipation and intermittency in turbulence at very high Reynolds numbers, Proc. R. Soc. A **476**, 20200591 (2020).

[31] G. Elsinga and I. Marusic, Universal aspects of small-scale motions in turbulence, J. Fluid Mech. **662**, 514 (2010).

[32] T. Ishihara, Y. Kaneda, and J. C. R. Hunt, Thin shear layers in high Reynolds number turbulence-DNS results, Flow Turbul. Combust. **91**, 895 (2013).

[33] K. Horiuti and K. Fujiwara, The multi-mode stretched spiral vortex in homogeneous isotropic turbulence, J. Fluid Mech. **595**, 341 (2008).

[34] K. Yoshimatsu, K. Anayama, and Y. Kaneda, Influence of vortex dynamics and structure on turbulence statistics at large scales, Phys. Fluids **27**, 055106 (2015).

[35] https://macc.fccn.pt.

[36] http://www.lca.uc.pt.

[37] http://www.2decomp.org/.